ORIGINAL PAPER

Border-independent multi-functional, multi-hazard exposure modelling in Alpine regions

M. Pittore[1] · P. Campalani[1] · K. Renner[1] · M. Plörer[2] · F. Tagliavini[3]

Abstract

Extreme hydrometeorological events such as the 2018 Vaia storm increasingly threaten alpine regions with multiple hazards often compounded and with cascading effects. Currently available risk assessment and prevention tools may therefore prove inadequate, particularly for transborder and vulnerable mountain areas, calling for comprehensive multi-hazard and transdisciplinary approaches. In particular, the exposed assets should not anymore be considered a sheer collection of static items, but the models should also reflect functional features. In this paper, we propose an integrated approach to multi-hazard exposure modelling including both static and functional components. The model is based on a homogeneous planar tessellation composed of hexagonal cells and a graph-like structure which describes the functional connections among the cells. To exemplify the methodology, a combination of static (buildings, protective forests), dynamic (population) and functional (road-based transport system) components has been considered together, targeting a ca. 10,000 km^2 region across Italy and Austria. A cell-based aggregation at 250 m resolution and an innovative graph-based simplification allow for a good trade-off between the complexity of the model and its computational efficiency for risk-related applications. Furthermore, aggregation ensures protection of sensitive data at a scale still useful for civil protection. The resulting model can be used for different applications including scenario-based risk analysis and numeric simulation, probabilistic risk assessment, impact forecasting and early warning.

Keywords Exposure · Risk · Multi-hazard · Flow · Traffic

✉ M. Pittore
mpittore@eurac.edu

1 EURAC Research, V.le Druso 1, 39100 Bolzano, Italy

2 Federal Research and Training Centre for Forests, Natural Hazards and Landscape (BFW), Seckendorff-Gudent-Weg 8, 1131 Vienna, Austria

3 Dipartimento Regionale per la Sicurezza del Territorio, ARPA Veneto, Via Tomea 5, 32100 Belluno, Italy

1 Introduction

Extreme hydrometeorological events such as late autumn and winter storms are being increasingly observed in southern Europe and particularly in the Alps (Gobiet et al. 2014), where they threaten environmental and socio-economic systems (Ulbrich et al. 2013). An example is the 2018 Vaia (also known as Adrian) storm, which strongly affected Italy, Austria, France and Switzerland (Giovannini et al. 2021). This storm has been considered exceptional yet could foreshadow complex phenomena with multiple hazards often compounded and with cascading effects, whose frequency and intensity are likely to be influenced by climate change (Bouwer 2019; Pinto et al. 2012).

Furthermore, such high-intensity hydrometeorological events can extend to large, even synoptic scale events, often adversely affecting neighbouring countries in the same time frame. In such conditions, available approaches and tools may fall short of addressing risk assessment and prevention that are border-independent and in vulnerable mountain regions (Martin et al. 2015), also considering climate change. It is therefore paramount to support the Civil Protection Departments and the local and national authorities to improve risk management for complex events and being able to collaborate on risk assessment (and subsequently on DRR actions).

As hazards are affecting people, physical assets and functions directly and indirectly in an interconnected living space, also risk management (preparedness and response) needs to work border-independently. By developing a border-independent exposure model, we provide one key component to assess the risk of a region, which is the basis for preparedness action.

In the framework of risk management (related to specific natural events or to climate change), the assessment phase is usually including the evaluation of three main components, namely hazard, exposure and vulnerability (UNDRR 2022; UNISDR 2009). Exposure, in particular, aims at describing people, infrastructure, housing, production capacities and other tangible assets and systems located in hazard-prone areas and susceptible to be damaged (UNISDR 2009). In case of intense storms in alpine regions, multiple hazards are often compounded (e.g. strong winds and rain) leading to different cascading impacts (e.g. landslides, debris flows, fluvial floods) (e.g. Bouwer 2019). Even in such complex situations, a relatively small set of exposed assets is exposed to the most relevant risks (Pittore et al. 2017), notably including both static (e.g. buildings) and dynamic (people) components. Population is conventionally the most important exposure element to consider when analysing the risks of natural hazards. Whereas there is a long history of research into understanding and modelling hazards, determining exposure, and in particular dynamic exposure, only recently became a more researched topic resulting in several gridded high-resolution spatial datasets and model approaches being published (Aubrecht et al. 2014; Bhaduri et al. 2007; European Commission. Joint Research Centre 2022; Freire and Aubrecht 2012; Martin et al. 2015; Renner et al. 2018; Smith et al. 2016; Stevens et al. 2015). High-resolution gridded global datasets currently available such as Worldpop (Tatem 2017) represent static night-time population. Local administrations work with population per administrative areas or, as in some cases with number of people per residential address. However, people are highly mobile, which is often not considered in the analysis of exposure.

The range of impacting mechanisms, especially for intense hydrometeorological events, includes very often direct (physical) damages to assets, as well as indirect effects based on the functional impairment of the underlying systems. For instance, the interruption of a road caused by a landslide or a bridge collapse due to extreme river run-off can severely affect the emergency reaction capabilities and ultimately threaten the exposed communities (Dalziell and Nicholson 2001; Dave et al. 2021). This is particularly evident in rural and mountainous areas where the road network has little redundancy and is more exposed to natural hazards (Argyroudis et al. 2019; Dalziell and Nicholson 2001). This combination of direct and indirect effects is often not thoroughly considered in risk assessment activities.

Partly this issue might stem from the difficulty in integrating functional components into exposure models. In fact, although several research contributions over the last decades addressed the integration of roads risk assessment for several natural hazards (e.g. Anastassiadis and Argyroudis 1991; Argyroudis et al. 2019; Dalziell and Nicholson 2001; Ganin et al. 2017; Lam et al. 2018), to date there are no approaches able to integrate transport infrastructure, population and other assets into a single, actionable structure. Transport infrastructures are often complex, and their representation does not scale well while increasing the geographical scope of the models. On the other side, including such functional components into a model would allow to model not only the static spatial distribution of exposure (e.g. people) but also their flow dynamics, which is usually constrained on the underlying road network.

The purpose of this paper is to foster the discussion on exposure modelling for complex hydrometeorological events and propose a novel approach to generate multifunctional exposure models able to improve multi-hazard comprehensive risk assessment. The approach aims at seamlessly integrating functional components (starting with road networks) into static exposure models. This allows to account for more complex impacts and damage and loss mechanism without increasing the complexity of the model. The approach is based on the use of a hexagonal planar tessellation, which provides the basis for spatial aggregation, and its dual graph representation, onto which the underlying road network is projected by a simplification process. The model allows to model flows (e.g. of people or vehicles) as well as their spatial distribution in a simple and consistent spatial framework, which can be populated with different exposure elements from heterogeneous data sources. This information—along with other exposure datasets co-aligned onto the same tessellation—enables for a much more realistic risk assessment on the regional level (e.g. to test and validate extensive border-independent disaster scenarios and related emergency management, including evacuation) and represents a useful element for a potential multi-hazard pre-operational/early warning system. By quantifying the ability of the system to maintain its level of service—or to restore itself within a certain amount of time—upon one or more disruptions caused by, for example, damaging hazards, a better estimate of its vulnerability/resilience could also be obtained. Furthermore, the proposed approach can be generalized to other exposed systems (e.g. water and power infrastructures) which play an important role in the analysis of systemic risk.

In Sect. 2, the study area and input datasets are described; the detailed steps of the exposure model calculation are subsequently listed in Sect. 3; in Sect. 4, the main results are presented and discussed, also considering potential practical applications of the proposed approach; Sect. 5 discusses the applicability and limitations of the model, while in Sect. 6 conclusions and outlook are discussed.
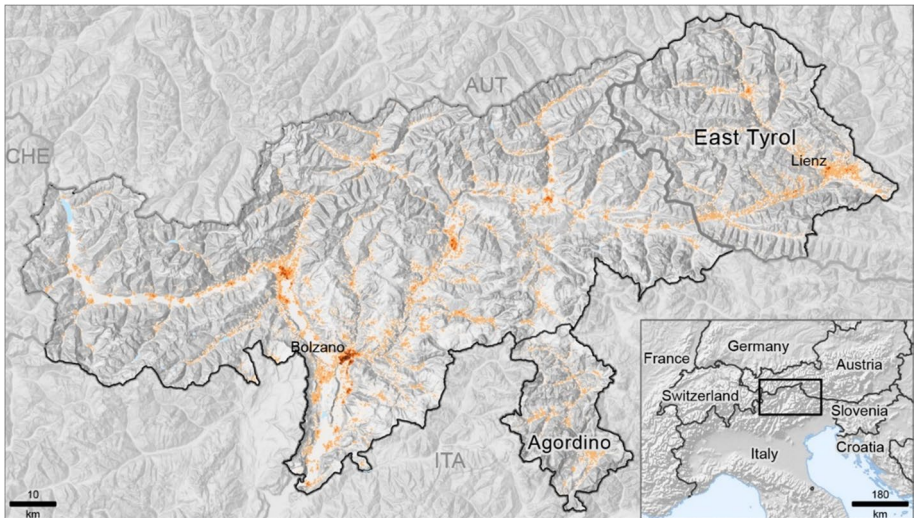
Fig. 1 Map showing the study area consisting of the Autonomous Province of Bolzano South Tyrol (Italy), East Tyrol, part of the Austrian state of Tyrol and Agordino, a mountain community in the Italian Veneto Region. Population density is shown in yellow to red colours (low to high)

## 2 Study area and input data

The analysis was conducted in the European Alps covering the Italian province of South Tyrol, the Austrian region of East Tyrol and the mountain community of Agordino, a part of the Italian Veneto Region (Fig. 1). Individual steps of the methodology were applied to the South Tyrol only.

The following types of assets were considered in the exposure model presented in this paper: buildings, population, health sites, education facilities, tourist accommodations, protection forest, sealed surfaces, forested areas and road network (Table 1). Where the required information was not available from official sources, they were gathered from global datasets. No harmonization was required of the datasets from regional administrations. Preprocessing of the data was required for representing population at a 250 m spatial resolution for East Tyrol and Agordino. Very high-resolution data on resident population were readily available at the address level from the authorities of the Autonomous Province of Bolzano. For Agordino and East Tyrol, gridded population distribution was created by disaggregating the most recent population figures per municipality to building locations using the freely available GHS-POP2G tool (European Commission. Joint Research Centre 2020).

Data on movements of people from resident to workplace locations were available for the Autonomous Province of Bolzano. The information was presented as a set of point-to-point trip units, for a total of around 260,000 commuting population, which is about half of the resident population in South Tyrol (512,000 ca.). This very high-resolution commuters dataset was aggregated through an iterative Voronoi space partitioning to a minimum of 200 people per resident/workplace over 250 m hexagonal cells; where this minimum criterion did not apply, i.e. in rural areas, larger Voronoi cells were created, as shown in Fig. 2. This preprocessing was a necessary step to achieve the anonymization/privacy level required to share the data. Each set of people has a unique identifier assigned allowing to

Table 1 Listing of the exposure datasets that were aggregated onto the common hexagonal tessellation at 250 m of resolution ($\mathcal{H}_{250}$) over the cross-border study area including South Tyrol (IT), Agordino (Veneto, IT) and East Tyrol (AU)

#	Name	Description	Unit	Source
01	Buildings	Number of buildings	–	OpenStreetMap, 2021; Veneto regional administration, 2022; Tyrol regional administration, 2003
02	Buildings	Area covered by buildings	m^2	OpenStreetMap, 2021; Veneto regional, 2022; Tyrol regional administration, 2003
03	Population	Number of people	–	Autonomous Province of Bolzano, 2022, Italian National Statistical Office, 2021; Austrian National Statistical Office, 2019
04	Hospitals	Number of health facilities	–	Autonomous Province of Bolzano, 2022; OpenStreetMap; 2022
05	Schools	Number of education facilities	–	Autonomous Province of Bolzano, 2022; OpenStreetMap, 2022; Tyrol regional administration, 2021
06	Tourist accommodation	Number of hotels and guesthouses	–	Autonomous Province of Bolzano, 2022; OpenStreetMap, 2022
07	Protection forest	Proportion of the cell covered by protection forest	%	Autonomous Province of Bolzano, 2013; Veneto regional administration, 2009; Tyrol regional administration, 2021
08	Artificial surface density	[0, 1] area density of artificial surfaces (CORINE Level 1 attribute equal to 1)	1	CORINE Land Cover 2018
09	Forest surface density	[0, 1] area density of forest and semi-natural areas (CORINE Level 1 attribute equal to 3)	1	CORINE Land Cover 2018
10	Main roads	Length of main roads (OSM *highway* tag in {`motorway`, `motorway_link`, `trunk`, `trunk_link`, `primary`, `primary_link`})	m	OpenStreetMap, 2022
11	Other roads	Length of roads not included in #10 (secondary, tertiary and so on)	m	OpenStreetMap, 2022
12	Commuter flow	Flow of no. of residents from home to work	–	Autonomous Province of Bolzano, 2019
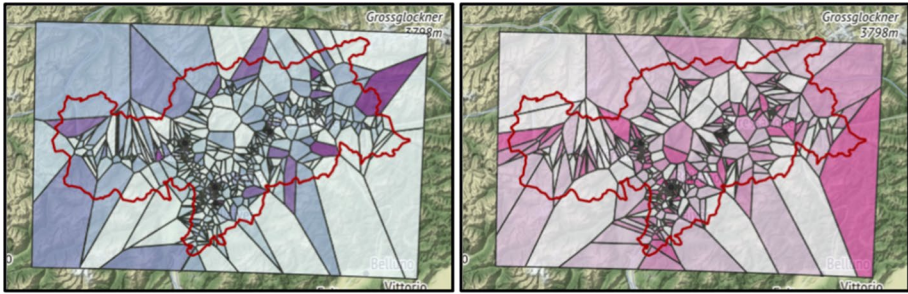
Fig. 2 Source ($\mathcal{T}_S$, on the left) and target ($\mathcal{T}_T$, on the right) tessellations used by Arbeitsmarktbeobachtung/Ufficio Osservazione Mercato del Lavoro of Bozen/Bolzano. The colour gradient is used to encode total number of outgoing/ingoing trips fr each location

calculate flows of N number of people from resident cells to work cells. For East Tyrol, data on commuter's resident and workplace location were available as number of people per 250 m square cell. However, the relationships between resident and work cells were not known; thus, actual movements could not be derived.

Land-cover–land-use information was extracted and aggregated from the latest Copernicus "CORINE Land Cover" dataset (CLC 2018). Data on road infrastructure were extracted from the OpenStreetMap (OSM) database via *OSMnx* Python library (Boeing 2017).

Table 1 presents the complete list of exposure datasets that were harmonized and used for this study.

3 Methodology

The proposed methodology is based on the integrated modelling of functional and non-functional components of exposure in planar tessellations (i.e. set of non-overlapping polygonal cells that completely cover a surface). It is assumed here that several non-functional components (physical assets) of relevance for exposure (Promper and Glade 2016) can be efficiently aggregated by means of different summary statistics onto a set of polygonal cells (Pittore et al. 2020), as described in Sect. 3.1. Each polygonal tessellation has a natural dual graph representation, which inherits the connectivity of the generating polygons. We note that also functional components such as transport infrastructure can, in most cases, be represented by spatial graphs, i.e. a set of vertices connected by edges (Dave et al. 2021). Since such graph structures can be remarkably complex, they can be conveniently simplified by projecting and aggregating them onto the dual graph of the tessellation. The connectivity between the polygonal cells is therefore defined by their capacity to let people and cars to move across their boundaries (see Sect. 3.3). This allows to consider the cells of the exposure model not only as separate geographical entities describing aggregated properties of the underlying territory, but as organic parts of a connected system.

3.1 Exposed elements and systems

The analysis presented here uses the Vaia storm event from 28 to 30th October 2018 heavily impacting the study area, as an example of a multi-hazard severe weather event with compound and cascading effects. The exposed elements considered in the model
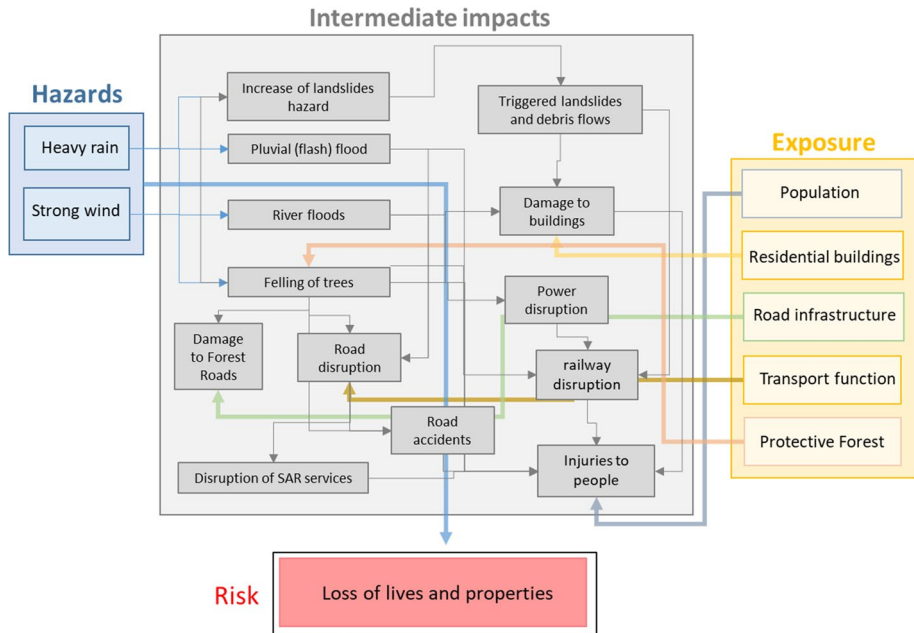
Fig. 3 Impact chain (partial) of a storm event. On the left side, the two considered hazards. On the right side, the exposed assets and functions which are possibly exposed to damage and loss from the direct and indirect impacts (depicted in the central area). All components contribute to the main risk of losing lives and properties. We note that the vulnerability component is not shown

were determined based on impact assessment following Vaia. A partial conceptualization of the impacts that can be observed in case of a strong storm is shown in Fig. 3 in the form of an *impact chain* (Zebisch et al. 2021). This representation provides a visual depiction of the different chains of intermediate impacts linked to two different hazards which are usually observed compounded in the event of a strong storm, namely heavy rain and strong wind. Most of these impacts eventually contribute to the risk of losing lives and/or damaging assets and systemic functions (the vulnerability component is not considered here for the sake of simplicity). Each impact is associated with a different exposed asset or function, which can be negatively affected, directly or indirectly, by the hazards.

Three days of strong winds, heavy rainfall, increased surface run-off at higher altitudes and compounding mass movements caused severe and extensive damage to forests, injuries and some fatalities, damage to buildings and communication, power and transport infrastructure. The extensive windthrows affected also protection forests, which is of concern also in the longer term as it might increase the risk of gravitational mass movements. By analysing the impact chains and considering the main hazards associated with extreme hydrometeorological events (heavy rain, strong snowfall, strong wind) and the possible direct and indirect impacts, the 12 informational layers listed in Table 1 and describing the main exposed physical assets have been selected and aggregated at the level of individual polygonal cells. Among the exposed assets also, *protection forest* was considered, which indicates those forested areas that mitigate or prevent the impact of a natural hazard, including a rockfall, avalanche, erosion, landslide, debris
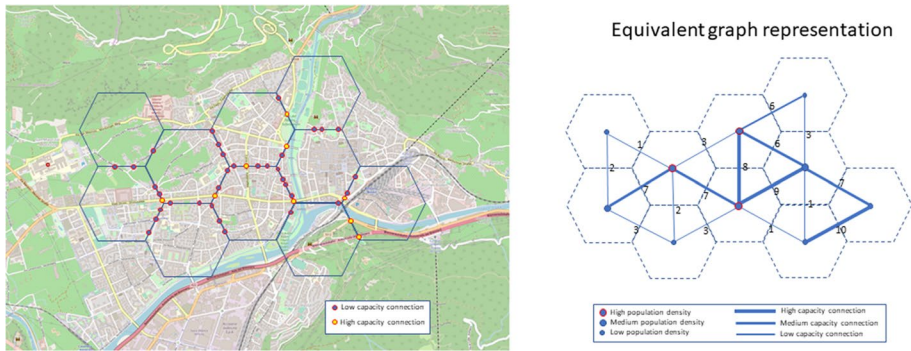
Fig. 4 Example of mesh-based modelling (left) and equivalent graph representation (right). The numbers represent the nominal capacity of the arcs, obtained by summing up the capacity of the roads crossing the cells borders. The connection points are depicted on the left; low- and high-capacity connections contribute, respectively, with 1 and 5 to equivalent arc capacity

flow or flooding on people and their assets in mountainous areas. It can be noted that such layer can also be seen as a vulnerability component, depending on the specific application.

3.2 Geospatial integrated model

All available input datasets described in Sect. 2 were aggregated onto a common tessellation. This tessellation is composed of regular hexagons with height h—i.e. the centroid-to-edge orthogonal distance—of 125 m. The edge is then $h/\cos(\pi/6) \approx 145$m, and the edge-to-edge distance (akin to grid-equivalent resolution) is $2h = 250$ m. From now on, we will refer to this tessellation as $\mathcal{H}_{250}$. A resolution of 250 m was picked as a good trade-off value between the existing requirements of both spatial accuracy and the handling of sensitive information. In order to deal with population flow over a roads network (but more in general to represent multifunctional exposure models), a hexagonal tessellation is deemed topologically more suitable than a common square grid (Birch et al. 2007): hexagons reduce the sampling bias due to their low perimeter-to-area ratio, they are close to circular shape and hence better reproduce curves, and neighbouring locations are all at the same distance from the cell. Hexagonal grids provide a higher spatial resolution than square grids and suffer less from orientation bias (Mersereau 1979). A tessellation of regular hexagons is also a Voronoi diagram; hence, all points within a hexagon are closest to its centroid than any other Delaunay/centroid point in the region, implying a better spatial representativeness of each cell.

3.3 Equivalent transportation model

Starting from the original graph of OpenStreetMap drivable roads G_{OSM}, we computed the equivalent simplified graph—which we will call G_{250}—by projecting it onto our $\mathcal{H}_{250}$ tessellation. As depicted in Fig. 4, the simplification algorithm computes the number of roads hitting the border between two cells (hexagons) h_u and h_v of the tessellation and sets it as attribute n_{uv} of the edge $\underline{e}_{uv}$ connecting the cell's centroids. A weight C_{uv} is also attached to

each edge, computed as a weighted linear combination of the weight of each hitting road. Such weighting scheme reflects the capacity of a road; hence, primary roads take more weight than secondary roads, which weigh more than tertiary roads, and so on.

Implementation-wise, we downloaded the OSM data with the *OSMnx* Python library, which includes algorithms for transforming the original roads network to a proper directed graph. Further computations on the graph were implemented with the Python *NetworkX* graph library, its natural companion. With regard to performance, the software we implemented for generating the results presented in this paper is not ready for near real-time operational adoption, and a round of optimization will be required. Internal algorithms—although partially parallelized and generally designed for scalability at wider geographical scales and/or higher resolutions—can be further improved to achieve better asymptotic upper bounds of performance cost. The *NetworkX* library we used for the low-level subroutines is also not optimal with respect to other existing Python packages,[1] despite being actively maintained at the time of writing; thus, it will be considered for replacement in the future.

3.4 Dynamic population modelling

In order to achieve a preliminary dynamic modelling of population, three main time frames were identified: daytime, night-time and commuting (as already employed in disaster risk assessment). The main hypothesis was that night-time population is well represented by resident (census-based) population, while daytime population strongly depends on the spatial location of the registered employers in the considered region. In the commuting time frame, the assumption was that all people will move from home their workplace (and vice versa). In both daytime and commuting time frames, it was assumed that the people not employed will stay at home (generating therefore a background value against which the dynamic component is evaluated).

It can be noted that the above are strong assumptions, considering for instance that—especially in the last years—a significant share of people might work at home or move around as part of their work duties. Furthermore, for the sake of simplicity we did not consider the contribution from schools, where pupils are spending several hours every day (see the outlook activities in the concluding section). Additionally, the model describes a typical work week (Monday to Friday).

To evaluate the daytime and commuting component, a dataset of home/work commuting trips $Y = \{y(l_i, l_j)\}$ of South Tyrol was provided by the *Amt für Arbeitsmarktbeobachtung/Ufficio Osservazione Mercato del Lavoro* of Bozen/Bolzano, recorded over December 2019, along with the local resident and employees datasets, as described in Sect. 2. In order to project this dataset to the $\mathcal{H}_{250}$ tessellation, we distributed the original trip information based on a simple probabilistic approach, driven by the resident and employee population m_k/e_k distribution on the hexagonal cells: one trip in the source dataset was projected as an $N \times M$ set of virtual trips, N and M being the number of cells that were selected in the original source ($\mathcal{T}_S$) and target ($\mathcal{T}_T$) Voronoi diagrams (visualized in Fig. 2). The selection of the source N cells was driven by the m_k residents, while the selection of the target M cells by the e_k employees. The resulting downscaled dataset,

---

[1] https://www.timlrx.com/blog/benchmark-of-popular-graph-network-packages.

Table 2 Pseudo-dynamic population modelling of a location h_i at different time units on working days (Mon–Fri): t_1 = home/work morning commute; t_2 = daytime; t_3 = work/home afternoon commute; t_4 = night-time. $\bar{y}(h_u, h_v)$ represents a normalized flow information between locations h_u and h_v where the shortest path on graph passes through h_i; m_i/e_i is the residents/employees population aggregated on location h_i; and O_i is the total output flow of location h_i, equal to $\sum_j \bar{y}(h_i, h_j)$

	t_1 5AM–9 AM	t_2 9AM–6PM	t_3 6PM–8PM	t_4 8PM–5AM
$m_i(t_n)$ Mon–Fri	$(m_i - O_i) + \sum \bar{y}(h_u, h_v)$	$(m_i - O_i) + e_i$	$(m_i - O_i) + \sum \bar{y}(h_u, h_v)$	m_i

i.e. the commuting share of the population, is thus a set of *estimated* trips $\{\hat{y}(h_i, h_j)\}$ connecting point-to-point two hexagonal cells of $\mathcal{H}_{250}$, each.

The subsequent step was to project the commuting flow onto the simplified/tessellated road network graph G_{250}. In order to do so, $r(h_i, h_j) = \{e_n\}$ being the shortest path between the cells h_i and h_j on the graph, then the correspondent flow $\hat{y}(h_i, h_j)$ was cumulatively added to each of the edges e_n in the path. This procedure was executed for each pair available in the dataset. Being R the number of edges in $r(h_i, h_j)$, then the normalized population flow attached to each single edge e_n in the path was also computed as $\bar{y}(h_i, h_j) = \hat{y}(h_i, h_j)/R$.

The routing on graph was calculated with the well-known Dijkstra shortest path algorithm via the *NetworkX* Python library (Hagberg et al. 2008). The cost c_n attached to each edge was set to the inverse of its capacity C_n, so to promote the use of main roads. In order to simulate the possible spreading of commuters onto alternative paths (e.g. due to increasing traffic on optimal connections), the cost c_n of each edge e_n can be updated after the processing of each trip in the following way[2]:

$$C_n^{k+1} = \max\left(1, C_n^k - \frac{\hat{y}(h_i, h_j)}{\oint r(h_i, h_j)}\right) \tag{1}$$

Dynamic edge capacity at iteration $k \to (k+1)$ for a generic edge $e_n \in r(h_i, h_j)$: the estimated flow of people $\hat{y}$ is normalized to the length of the shortest path r (expressed in km) and then subtracted from the actual capacity of the edge, while keeping a minimum capacity $C_n^{min} = 1$.

This option increases the complexity of the model: now in between the initial empty graph $G_{250} = G_{250}(k = 0)$ and the graph $\dot{G}_{250} = G_{250}(k = N)$ with all the N commuters data being projected onto it, there are intermediate states of the graph for each $k \in [1, (N-1)]$. This must be taken into account for any intermediate state of the graph, like the flow rerouting due to road interruptions described in Sect. 4.

The commuters' flow embedded in $\dot{G}_{250}$ was then combined with the data on residents and employees by the Province of Bolzano in order to obtain an estimate of the population's dynamics over a generic 24-hour timeframe in a workweek, subdivided into four time intervals (assuming that the morning and evening home-commuting flows are equivalent to $\dot{G}_{250}$), as exemplified in Table 2.

In the next section, we describe some of the results from the implementation of this procedure.

---

[2] Note that in this case, the processing of the available estimated flow pairs shall be in strict random order to minimize the bias on the state of the graph.
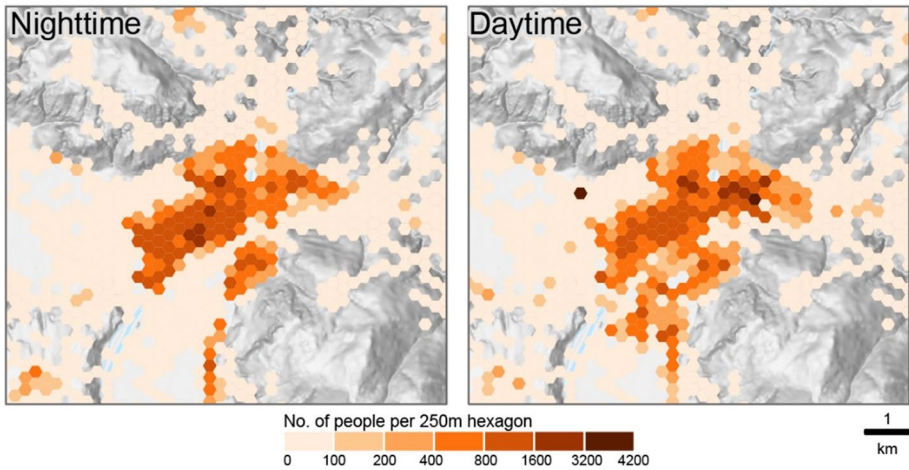
Fig. 5 Maps showing the night-time (left panel) and daytime population (right panel) on the $\mathcal{H}_{250}$ hexagonal mesh, for the Bozen/Bolzano (IT) area
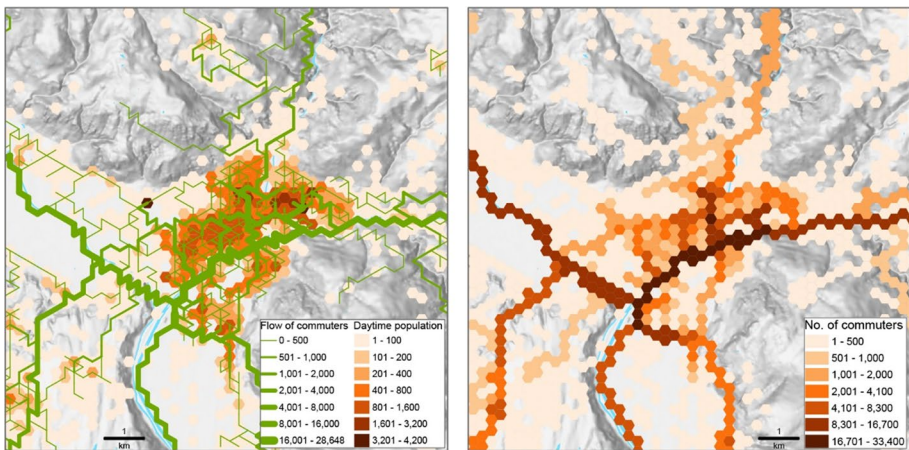

Fig. 6 Maps showing the flow of commuters along the graph and the daytime population (left panel) and the aggregate number of commuters on the H_250 hexagonal mesh

4 Results and applications

Figures 5 and 6 present a partial view of the resulting multi-temporal population model, aggregated on our common hexagonal grid $\mathcal{H}_{250}$. While the night-time population consists of the static resident population, the daytime population is the aggregation of people at workplaces (employees) and the residual resident population which are not involved in the commuting, as shown in Table 2.

Commuting population can be visualized in several ways: as both an overlay of the population at a given time and the actual commuting flow computed over the simplified roads network, or directly aggregated over the cells, with each cell representing the expected total
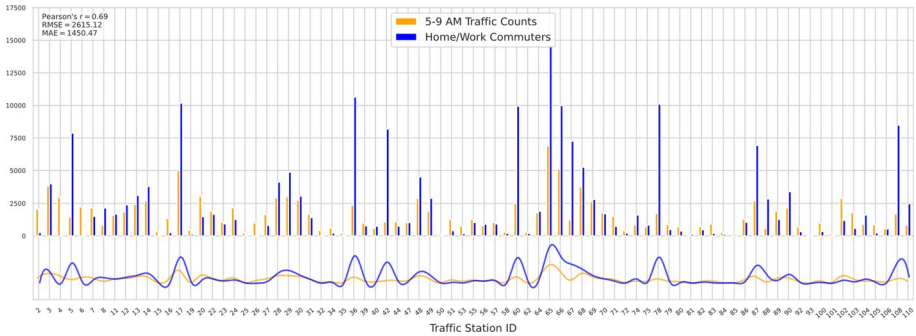
Fig. 7 Comparison between 2019 yearly averages of bidirectional traffic counts in South Tyrol in the time interval $t\_1 = 5$–9 AM and the commuting population flow. *RMSE* Root mean square error, *MAE* mean absolute error. Connecting (rescaled) splines are also shown in the $y < 0$ plane for clearer visualization of the results

flow, $\hat{y}$ (i.e. the total number of people expected to transit through the cell in the time frame), or the average number of people in transit during commuting, $\overline{y}$.

Comparing the original OSM roads graph G_{OSM} and its simplified tessellated counterpart G_{250}, we saw that the overall total lengths of all edges (roads) in both graphs were similar: 7907 km versus 7859 km. Indeed, the average number of roads bundled together in the simplified graph—$\sum n_{uv}/N$—is only 1.2 ca.: the low bundling rate, together with the zigzag effect that can happen on straight roads at certain bearing angles, can explain such results. However, looking at the number of roads intersections in both graphs, then we saw a significant decrease in complexity (55%), from 21,349 intersections in the original network to the 11,589 of G_{250}. This is most likely a consequence of the size of the hexagons, which tend to group together many roads intersections at the small scale of the cities and villages. The visual distortive effect of the tessellation on the roads network at such pseudo-resolution of 20 m is anyway only an interface-level artefact which does not affect the capabilities of the still available underlying network. Such connectivity graph—currently only representing the roads network of the study area—was purposely simplified and designed to host multiple sources of data that could be used for risk and emergency management, like electric grid or water supply pipes. On top of the simplified topology of the G_{250} network, the estimated (aggregated) population flow $\hat{y}(h_i, h_j)$—depicted in Fig. 6 over the area of Bozen/Bolzano—was compared with pre-pandemic traffic counts data in South Tyrol freely available from the Autonomous Province of Bolzano at https://astat.provinz. bz.it/.

The comparison is presented in Fig. 7, showing both the bidirectional traffic count value t_i and the maximum value of flow registered in the edges hitting the correspondent cell h_i: $\max_{j} \overline{y}(h_i, h_j) \forall j : \exists \underline{e}_{ij}$, paired together per each of the traffic stations. To filter out traffic counts not relevant for our analysis as much as possible—i.e. traffic of cars not involved in the work commute routes—the value t_i was calculated as the sum of the traffic counts in the morning commuting time from 5 to 9 AM (t_1 in Table 2).

The linear correlation between the traffic counts and the estimated commuting flow is around 0.7, with an average non-negligible absolute difference of about 1500 people. Looking at the bar plot in Fig. 7, we can appreciate that this bias is resulting from the average between two different situations: (1) a reasonably well-fitting traffic simulation on certain stations and (2) considerably overestimating data on other stations. Figure 8
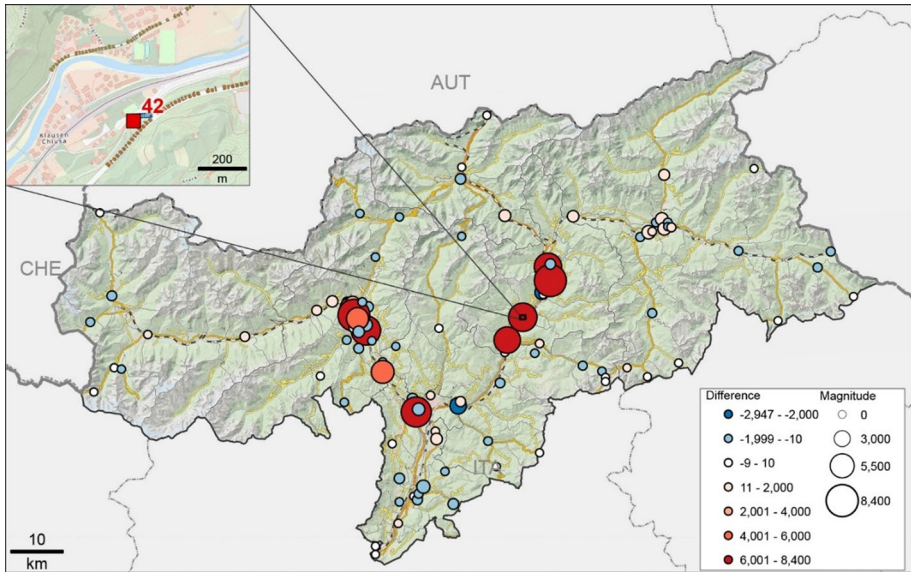
Fig. 8 Map showing the spatial distribution of the differences of the annual average 5–9 AM traffic counts and the modelled commuting flow near each of the traffic stations used in the comparison. Commuting flow overestimated is shown in red colours and underestimation in blue colours. The size of the circles is proportional to the magnitude of the difference value. The inset map shows traffic counting station number 42 located on state road SS12. Its location only 40 m distant from the motorway, which may explain the large discrepancy in modelled flow versus actual traffic

presents these discrepancies on a map, for each traffic station: as expected, larger estimation differences are found on edges with higher absolute flow of population, whereas areas outside the Meran-Merano/Bozen-Bolzano/Brixen-Bressanone triangle present less flow and consequently less estimation error.

Several potential applications of the proposed model can be devised, starting from the topological analysis on the simplified roads network graph G_{250}, where different vulnerability assessments are possible. Considering, for instance, the accessibility of the network to the closest hospital facility (i.e. distance on the equivalent graph), potentially vulnerable connection elements could be highlighted through a found indicator of road criticality such as the betweenness centrality, as shown in Fig. 9. Critical connections— i.e. playing a prominent role in the routing between the nodes of the graph and which can hardly be replaced by alternative routes—already flag out vulnerable parts of the transport network: by also assessing and co-locating the distance to the nearest hospital, we can further appreciate areas particularly prone to risk in case of roads interruptions due to, for example, extreme events.

Purely topological indicators may not always be representative and/or proportional to the actual population flow on it, so the availability of commuting flow estimations on the graph is a significant improvement towards a more realistic vulnerability assessment. This is especially the case for the evaluation of re-routed traffic and hence resilience of the network upon disruption of one or more roads, as shown in Fig. 10.

In order to exemplify the multi-hazard features of the proposed exposure model, we consider two different types of hazards relevant in the case of the 2018 Vaia storm (see
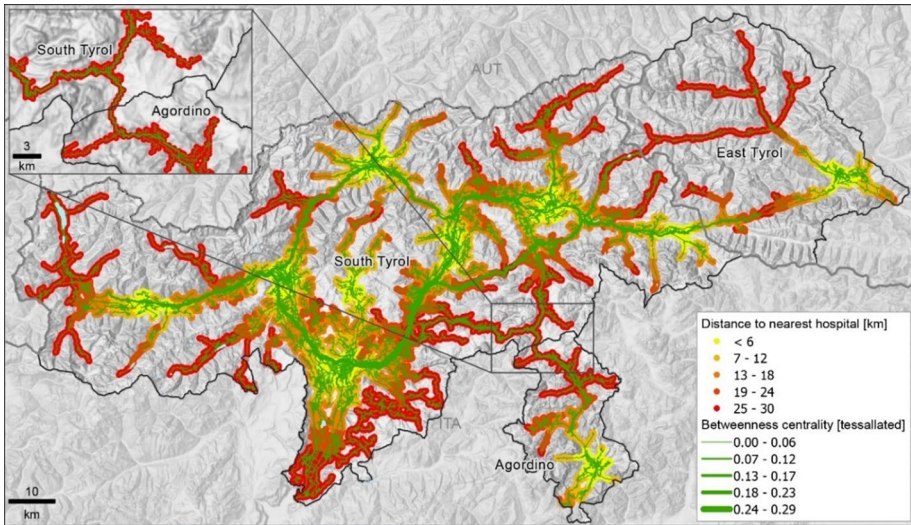
Fig. 9 Map showing the betweenness centrality topology indicator and the hospital accessibility for the study area. Critical parts of the roads network (bold green lines in the map) associated with difficult access to hospitals (yellow areas) can be considered potential proxies of vulnerable hotspots in case of road disruptions
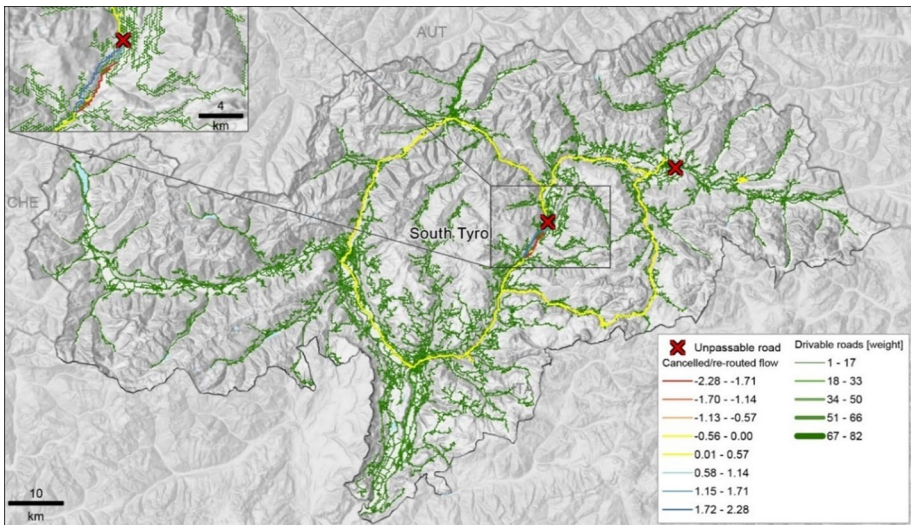
Fig. 10 Map showing an example of commuting flow re-routing simulation due to road disruptions that might, for example, be a direct consequence of a natural disaster

Fig. 3), namely strong winds and landslides triggered by precipitation. The two hazards were compounded during the 3-day event and led to serious consequences, including for instance the destruction of the protection forest, significant damage to roads and traffic interruptions. We consider here as hazard indicators for wind and landslides,

Table 3 Exposure values for the selected assets considering two separate and compound hazards with values exceeding 75th percentile, i.e. 15 m/s wind speed and 0.7 landslide susceptibility (defined over a [0,1] range)

Exposed assets (unit of measurement)	Wind (%)	Landslides (%)	Wind & landslides (%)
Residential buildings (number)	9′227 (5.4%)	12′414 (7.3%)	1′776 (1%)
Residential built-up area (m^2)	1.6e+6 (4.2%)	2.1e+6 (5.4%)	261′611 (0.7%)
Population (residents, number)	12′149 (2.3%)	18′412 (3.5%)	2′036 (0.4%)
Hospitals (number)	0	0	0
Schools and other educational (number)	22 (2.6%)	36 (4.2%)	6 (0.7%)
Elderly homes (number)	0	0	0
Tourist accommodations (number)	1′181 (11.7%)	801 (7.9%)	120 (1.2%)
Protection forest (ha)	25′588 (12.4%)	28′251 (13.7%)	5′758 (2.8%)
Roads (*main* and *other*, km)	322 (4.7%)	674 (9.7%)	64 (0.9%)

Table 4 Exposure values for the selected assets considering two separate and compound hazards with values exceeding 90th percentile, i.e. 19 m/s wind speed and 0.81 landslide susceptibility (defined over a [0,1] range)

Exposed assets (unit of measurement)	Wind (%)	Landslides (%)	Wind & landslides (%)
Residential buildings (number)	1′724 (1%)	2′756 (1.6%)	63 (0.04%)
Residential built-up area (m^2)	227′057 (0.5%)	471′237 (1.2%)	3′734 (0.01%)
Population (residents, number)	466 (0.09%)	3971 (0.7%)	0
Hospitals (number)	0	0	0
Schools and other educational (number)	0	5 (0.6%)	0
Elderly homes (number)	0	0	0
Tourist accommodations (number)	78 (0.8%)	185 (1.8%)	1 (0.01%)
Protection forest (ha)	7200 (3.5%)	7400 (3.7%)	700 (0.3%)
Roads (*main* and *other*, km)	47 (0.7%)	155 (2.2%)	1.1 (0.02%)

respectively, the maximum value of hourly 10 m wind speed module computed from the ERA5 downscaled reanalysis dataset (Raffa et al. 2021) and the maximum value of rain-triggered susceptibility to shallow landslides computed following the approach proposed by (Steger et al. 2023), both in the time frame from October 28, 2018, to 30, 2018, in the Trentino and South Tyrol region. Only the values exceeding the 90% percentile of the hazard distribution have been considered in order to estimate exposure to possibly damaging conditions. The exposure values for all considered assets (i.e. the so-called elements at risk) exceeding the 75th and 90th percentile of the hazard distributions are listed, respectively, in Tables 3 and 4. The values are computed by summing all exposure values in hexagonal cells whose location meets or exceeds the considered hazard values. Hazard associated with the cells have been defined in terms of the average value across the cell's surface.

It is possible to note that most exposed assets in case of the Vaia event were protection forests and roads, with, respectively, around 7200 and 700 ha of forest exposed to individual and compound extreme hazards. This is compatible with the observed damage actually incurred estimated in 1.5e6 m^3 of windthrow over around 6000 ha and around 342
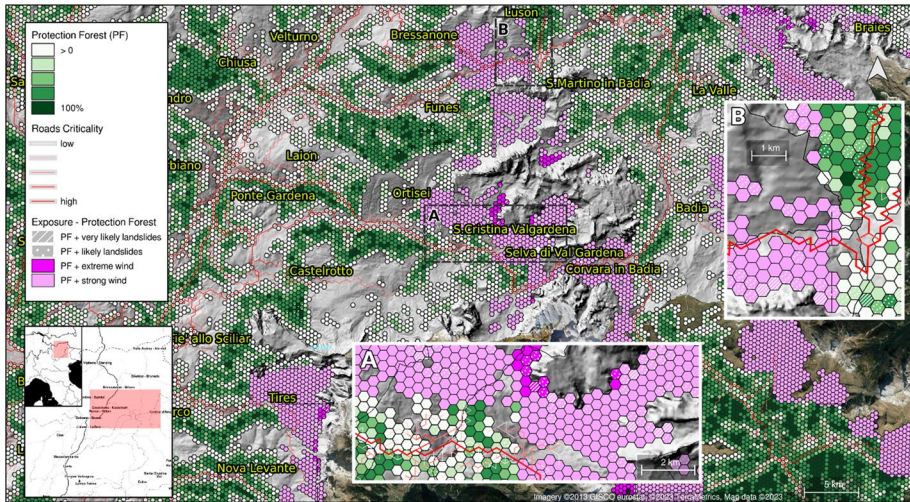
Fig. 11 Spatial distribution of protection forest and roads exposed to strong winds and high susceptibility to shallow landslides. The different colours and hatching represent possible combinations of multi-hazard exposure. Roads are colour-mapped according to their expected criticality

roads affected (Autonome Provinz Bozen 2019). Although no critical asset was exposed to extreme compound hazards, almost 4000 resident people were possibly exposed to landslides. These two specific exposed assets (protection forest and roads) are also considered for visualization, as shown in Fig. 11, where strong wind and likely landslides refer to hazard values exceeding the 75th percentile of the distribution while *extreme wind* and *extremely likely landslides* refer to values exceeding the 90th percentile. Roads are represented in terms of the alternative simplified graph defined over the tessellation and colour-mapped according to the expected degree of criticality (described by the topological *betweenness centrality* indicator).

The most exposed areas are often in arduous places, located at medium–high altitude and with consistent slope values. This explains the (fortunately) low number of casualties incurred in the region during the event.

5 Discussion

The consideration of different hazards from the perspective of exposure is multi-fold and rooted into the broader topic of multi-hazard and multi-risk assessment (e.g. Kappes et al. 2012), although in the literature this topic has been given comparably less attention. In fact, to consistently support multi-hazard (and multi-risk) assessment, exposure models should take into account already at design stage which structural and functional elements might be at risk, depending on a range of hazards whose spatiotemporal footprint can greatly vary in practical applications (Merz et al. 2020; Pittore et al. 2017). In this context, a selection of relevant physical systems and functions should be systematically carried out by analysing the pattern and cascade of observed (or possible) impacts. The use of impact chains (Zebisch et al. 2022) has been effective in better understanding the relationships between hazards and impacts and highlighting the relevant exposed

assets and systems subject to the often complex and extreme events in mountain regions (e.g. Zimmermann and Keiler 2015).

The different degree of exposure of the assets is not explicitly accounted for in the exposure model since it is mostly depending on the specific consideration of the hazard component in the assessment of risk. Therefore, the exposure model described in this work is multi-hazard in the sense that can be used to assess risk related to multiple hazards, either individually or compounded, as exemplified with two different relevant hazards in the case of the 2018 Vaia event. However, several design choices of the exposure modelling might affect its performance in multi-hazard applications. For instance, often exposure models are defined on aggregation boundaries either based on administrative borders as, for example, in (Pagliacci 2019), or on grids or other regular tessellations (e.g. Crowley et al. 2018) and the average size and shape of the boundaries plays a role in the subsequent risk assessment (Gomez-Zapata et al. 2021). Considering the expected spatial footprints of considered hazards and the distribution pattern of exposed elements, a hexagonal tessellation with equivalent grid size of 250m provided a good trade-off between model's complexity and spatial resolution.

Populating a border-independent model with data meant a somewhat greater effort in data collection. Data portals from three regional agencies in two different countries had to be navigated, searched, data downloaded and quality-checked. Where necessary, the dataset format and coordinate systems were harmonized into a common format. Moreover, in the case of data of population distribution additional data processing was conducted for the two regions where detailed data on disaggregated population distribution were not available. Compensating for lack of data in some regions with data from OpenStreetMap was straightforward, although quality and reliability of the data might differ. We decided to use authoritative data whenever possible as firstly they are considered higher quality than global datasets for the study area, and secondly, there may be a greater possibility of model results being taken up by the local authorities for risk assessment purposes.

The proposed graph simplification and aggregation scheme provides with an exposure model able to convey topological information and hence address the functional performance of the transport infrastructure along with information on spatial distribution of the physical asset. This comes at the expense of spatial resolution of the model itself, which is now defined uniformly by the size of the hexagonal cells of the tessellation. While this might be an issue for local assessment of small-area events (i.e. whose footprint size is significantly smaller than 250 m), the intended purpose of the model is rather to support larger-area impact forecasting and scenario-based risk assessment.

The estimation of dynamic population components derived from commuter data presented acceptable correspondence with real traffic counters data (0.7 r ca., Fig. 7), but there is clearly room for improvement on some aspects of the model. In the first place, we did not compare strictly equivalent numbers: persons on the one side and cars on the other. We cannot assume that each car carries just one person, and we do not know the statistical distribution of persons per car in the study area. The negative effect of this unknown variability in the final model is not straightforward to analyse, and the error might not be negligible. Moreover, there is also not always a direct spatial correspondence between the model and the traffic counters due to the simplifying view of the tessellation. All roads hitting the border between two contiguous hexagons are bundled together, and the load of simulated population flow they carry was then compared to the data of traffic stations. Such bundling might partially jeopardize the results especially difficult in those cells where a highway and a primary road get merged as a single tessellation link. This scenario is highlighted in the

inset of Fig. 8, where a traffic station in the SS12 primary road gets compared with a flow that also accounts for the A11 highway.

Even though the results of the first validation might be considered acceptable, several segments of population are not accounted for in the model, such as regular non-work-commuters traffic flow, tourists or external sources of traffic (as is especially the case of our study area where flow of lorries along the A22 highway is particularly intense).

Temporal variability at different scales is also a point for improvement in the model: from seasonal changes in traffic patterns, to weekend/weekdays differentiation, up to the modelling of near real-time traffic congestions and the re-routing options.

All these aspects are being analysed for the development of the next milestone of the model, which would bring the model from being a first showcase to a more operational service. Started as a so-called *evolutionary prototype*, the current state of implementation supports the core (and thus more basic) functionality: future releases—also driven by feedback and features wish lists from local consumers from both public and private sectors—will expand and refine the model towards a more consistent tool for Disaster Risk Management. The applicability of the model outside of the geographical boundaries of the study area—now restricted by the proprietary and local nature of the datasets provided by the Autonomous Province of Bolzano (as explained in Sect. 2)—will also be overcome at such stage by replacing them with statistical models.

6 Conclusions and outlook

This article presents a novel approach to design and implement a multifunctional exposure model for a border-independent multi-hazard risk assessment. The proposed approach stems from the consideration that exposed assets should be consistently represented in actionable frameworks including both static (e.g. buildings, forest) and dynamic (people) physical components and addressed also from the functional perspective. To exemplify the approach, the road transport infrastructure has been integrated into the model to support the estimation of multi-temporal population exposure. The resulting model is defined over a 250 m regular hexagonal tessellation which provides the support both for spatial aggregation of physical assets and for the topological and functional description of the underlying roads network. The latter is, in fact, projected onto the dual graph of the tessellation through a simplification procedure which decreases the complexity of the model while preserving the main features of the network. In future, such approach could be employed to integrate other infrastructure (e.g. water, energy grid). We also note as the generalized multi-flow commodity problem which underlies this application is NP-complete for integer flow, but solvable in polynomial time for fractional flow (Even et al. 1975), therefore theoretically allowing for an easier extension to other types of transport-type infrastructure relevant for risk assessment. The approach has been exemplified considering exposure to different hazards of concern in alpine regions, namely shallow landslides and strong winds, that can be compounded in case of extreme hydrometeorological events, as observed during the 2018 Vaia event. The resulting exposure model covers a cross-border 10,000 km^2 area between Italy and Austria, allows for a reasonable trade-off between spatial resolution, computational performance and scalability, and is oriented towards large-area multi-risk assessment.

The model provides a rich and multifaceted description of a complex territory in terms of residential buildings, location of schools, hospitals and touristic infrastructure, as well

as forests (which also act as significant protective element, against natural hazards). The multi-temporal population distribution implemented in the model has been preliminarily validated through comparison with measured traffic counts with promising results. Future updates of the model will include the integration of further information on the building stock (e.g. main materials) and on the demography and sector of work of the exposed population. The proposed approach would also benefit from the consideration of non-commuting population flow, improved urban traffic simulations, and the integration of other sources of information at local and regional level for calibration and testing. Such a calibrated model could then be reasonably extrapolated to other areas with similar topological and socio-economic profiles, like the Alpine region. Gravity models (Jiang et al. 2021) and neural networks (Jiang and Adeli 2003) will be considered to this purpose.

Finally, thanks to its spatial resolution and dynamic features, such an exposure model can be efficiently coupled with hazard models of the region (e.g. landslides susceptibility maps) and related vulnerability factors, and actively integrate the development of multi-hazard impact forecasting systems (Merz et al. 2020).

Authors' contributions MP, PC and KR contributed to the study conception and design. Material preparation, data collection and analysis were performed by PC, KR, MP and FT. The first draft of the manuscript was written by MP, PC and KR, and all authors commented on previous versions of the manuscript. All authors read and approved the final manuscript.

Data and code availability The Python modules developed to obtain the results shown in this paper are publicly available under the GNU GPLv3 licence in our institution's GitLab,[3] while sample maps of the presented model can be viewed from the institution's Web GIS under the "TRANS-ALP Project – Public" group.[4]

Declarations

Conflict of interest The authors declare that they have no known competing financial interests or personal relationships that could have appeared to influence the work reported in this paper.

Ethics approval Not applicable.

Consent to participate Not applicable.

Consent for publication Not applicable.

---

[3] https://gitlab.inf.unibz.it/earth_observation_public/cdr/risk-tessellator/-/tree/v0.1.0.

[4] https://maps.eurac.edu/groups/group/trans-alp-project-public.

References

Anastassiadis AJ, Argyroudis SA (1991) Seismic vulnerability analysis in urban system and road networks. Application to the city of Thessaloniki, Greece. Seismic Vulnerability Anal Urban Syst Road Netw 2:287–301

Argyroudis SA, Mitoulis SA, Winter MG, Kaynia AM (2019) Fragility of transport assets exposed to multiple hazards: State-of-the-art review toward infrastructural resilience. Reliab Eng Syst Saf 191:106567. https://doi.org/10.1016/j.ress.2019.106567

Aubrecht C, Steinnocher K, Huber H (2014) DynaPop—Population distribution dynamics as basis for social impact evaluation in crisis management, in: ISCRAM 2014 Conference Proceedings. In: Presented at the 11th international conference on information systems for crisis response and management, pp 314–318

Autonome Provinz Bozen (2019) VAIA 2018 - VI. Report. Autonome Provinz Bozen Abteilung Forstwirtschaft

Bhaduri B, Bright E, Coleman P, Urban ML (2007) LandScan USA: a high-resolution geospatial and temporal modeling approach for population distribution and dynamics. GeoJournal 69:103–117. https://doi.org/10.1007/s10708-007-9105-9

Birch CPD, Oom SP, Beecham JA (2007) Rectangular and hexagonal grids used for observation, experiment and simulation in ecology. Ecol Model 206:347–359. https://doi.org/10.1016/j.ecolmodel.2007.03.041

Boeing G (2017) OSMnx: New methods for acquiring, constructing, analyzing, and visualizing complex street networks. Comput Environ Urban Syst 65:126–139. https://doi.org/10.1016/j.compenvurbsys.2017.05.004

Bouwer LM (2019) Observed and projected impacts from extreme weather events: implications for loss and damage. In: Mechler R, Bouwer LM, Schinko T, Surminski S, Linnerooth-Bayer J (eds) Loss and damage from climate change, climate risk management, policy and governance. Springer, Cham, pp 63–82. https://doi.org/10.1007/978-3-319-72026-5_3

Crowley H, Despotaki V, Rodrigues D, Silva V, Toma-Danila D, Riga E, Karatzetzou A, Fotopoulou S, Sousa L, Ozcebe S, Gamba P (2018) Interactive European exposure model gridded data viewer. Eur Seism Risk Serv. https://doi.org/10.7414/EUC-EUROPEAN-EXPOSURE-MODEL-GRIDDED-v0.1

Dalziell E, Nicholson A (2001) Risk and impact of natural hazards on a road network. J Transp Eng 127:159–166. https://doi.org/10.1061/(ASCE)0733-947X(2001)127:2(159)

Dave R, Subramanian SS, Bhatia U (2021) Extreme precipitation induced concurrent events trigger prolonged disruptions in regional road networks. Environ. Res. Lett. 16:104050. https://doi.org/10.1088/1748-9326/ac2d67

European Commission. Joint Research Centre. (2020) GHS-POP2G user guide: population to grid tool user guide: version 2.0. Publications Office, LU

European Commission. Joint Research Centre. (2022) GHSL data package 2022: public release GHS P2022. Publications Office, LU

Even S, Itai A, Shamir A (1975) On the complexity of time table and multi-commodity flow problems. In: Presented at the 16th annual symposium on foundations of computer science (sfcs 1975). IEEE, USA, pp 184–193. https://doi.org/10.1109/SFCS.1975.21

Freire S, Aubrecht C (2012) Integrating population dynamics into mapping human exposure to seismic hazard. Nat Hazards Earth Syst Sci 12:3533–3543. https://doi.org/10.5194/nhess-12-3533-2012

Ganin AA, Kitsak M, Marchese D, Keisler JM, Seager T, Linkov I (2017) Resilience and efficiency in transportation networks. Sci. Adv. 3:e1701079. https://doi.org/10.1126/sciadv.1701079

Giovannini L, Davolio S, Zaramella M, Zardi D, Borga M (2021) Multi-model convection-resolving simulations of the October 2018 Vaia storm over Northeastern Italy. Atmos Res 253:105455. https://doi.org/10.1016/j.atmosres.2021.105455

Gobiet A, Kotlarski S, Beniston M, Heinrich G, Rajczak J, Stoffel M (2014) 21st century climate change in the European Alps—a review. Sci Total Environ 493:1138–1151. https://doi.org/10.1016/j.scitotenv.2013.07.050

Gomez-Zapata JC, Brinckmann N, Harig S, Zafrir R, Pittore M, Cotton F, Babeyko A (2021) Variable-resolution building exposure modelling for earthquake and tsunami scenario-based risk assessment.

An application case in Lima, Peru. Nat Hazards Earth Syst Sci. Discuss 5:1–30. https://doi.org/10.5194/nhess-2021-70

Hagberg AA, Schult DA, Swart PJ (2008) Exploring network structure, dynamics, and function using NetworkX 5

Jiang X, Adeli H (2003) Freeway work zone traffic delay and cost optimization model. J Transp Eng 129:230–241. https://doi.org/10.1061/(ASCE)0733-947X(2003)129:3(230)

Jiang Y, Li Z, Cutter SL (2021) Social distance integrated gravity model for evacuation destination choice. Int J Digit Earth 14:1004–1018. https://doi.org/10.1080/17538947.2021.1915396

Kappes MS, Keiler M, Von Elverfeldt K, Glade T (2012) Challenges of analyzing multi-hazard risk: a review. Nat Hazards 64:1925–1958. https://doi.org/10.1007/s11069-012-0294-2

Lam JC, Adey BT, Heitzler M, Hackl J, Gehl P, van Erp N, D'Ayala D, van Gelder P, Hurni L (2018) Stress tests for a road network using fragility functions and functional capacity loss functions. Reliab Eng Syst Saf 173:78–93. https://doi.org/10.1016/j.ress.2018.01.015

Martin D, Cockings S, Leung S (2015) Developing a Flexible framework for spatiotemporal population modeling. Ann Assoc Am Geogr 105:754–772. https://doi.org/10.1080/00045608.2015.1022089

Mersereau RM (1979) The processing of hexagonally sampled two-dimensional signals. Proc IEEE 67:930–949. https://doi.org/10.1109/PROC.1979.11356

Merz B, Kuhlicke C, Kunz M, Pittore M, Babeyko A, Bresch DN, Domeisen DIV, Feser F, Koszalka I, Kreibich H, Pantillon F, Parolai S, Pinto JG, Punge HJ, Rivalta E, Schröter K, Strehlow K, Weisse R, Wurpts A (2020) Impact forecasting to support emergency management of natural hazards. Rev Geophys. https://doi.org/10.1029/2020RG000704

Pagliacci F (2019) Multi-hazard, exposure and vulnerability in Italian municipalities. In: Resilience and urban disasters. Edward Elgar Publishing, pp 175–198. https://doi.org/10.4337/9781788970105.00017

Pinto J, Karremann M, Born K, Della-Marta P, Klawa M (2012) Loss potentials associated with European windstorms under future climate conditions. Clim Res 54:1–20. https://doi.org/10.3354/cr01111

Pittore M, Wieland M, Fleming K (2017) Perspectives on global dynamic exposure modelling for geo-risk assessment. Nat Hazards 86:7–30. https://doi.org/10.1007/s11069-016-2437-3

Pittore M, Haas M, Silva V (2020) Variable resolution probabilistic modeling of residential exposure and vulnerability for risk applications. Earthq Spectra 36:321–344. https://doi.org/10.1177/8755293020951582

Promper C, Glade T (2016) Multilayer-exposure maps as a basis for a regional vulnerability assessment for landslides: applied in Waidhofen/Ybbs, Austria. Nat Hazards 18:111–127

Raffa M, Reder A, Marras GF, Mancini M, Scipione G, Santini M, Mercogliano P (2021) VHR-REA_IT dataset: very high resolution dynamical downscaling of ERA5 reanalysis over Italy by COSMO-CLM. Data 6:88. https://doi.org/10.3390/data6080088

Renner K, Schneiderbauer S, Pruß F, Kofler C, Martin D, Cockings S (2018) Spatio-temporal population modelling as improved exposure information for risk assessments tested in the Autonomous Province of Bolzano. Int J Disaster Risk Reduct 27:470–479. https://doi.org/10.1016/j.ijdrr.2017.11.011

Smith A, Martin D, Cockings S (2016) Spatio-temporal population modelling for enhanced assessment of urban exposure to flood risk. Appl Spat Anal Policy 9:145–163. https://doi.org/10.1007/s12061-014-9110-6

Steger S, Moreno M, Crespi A, Zellner PJ, Gariano SL, Brunetti MT, Melillo M, Peruccacci S, Marra F, Kohrs R, Goetz J, Mair V, Pittore M (2023) Deciphering seasonal effects of triggering and preparatory precipitation for improved shallow landslide prediction using generalized additive mixed models. Nat Hazards Earth Syst Sci 23:1483–1506. https://doi.org/10.5194/nhess-23-1483-2023

Stevens FR, Gaughan AE, Linard C, Tatem AJ (2015) Disaggregating census data for population mapping using random forests with remotely-sensed and ancillary data. PLoS ONE 10:e0107042. https://doi.org/10.1371/journal.pone.0107042

Tatem AJ (2017) WorldPop, open data for spatial demography. Sci Data 4:170004. https://doi.org/10.1038/sdata.2017.4

Ulbrich U, Leckebusch GC, Donat MG (2013) Windstorms, the most costly natural hazard in Europe. In: Boulter S, Palutikof J, Karoly DJ, Guitart D (eds) Natural disasters and adaptation to climate change. Cambridge University Press, Cambridge, pp 109–120. https://doi.org/10.1017/CBO9780511845710.015

UNDRR (2022) Technical guidance on comprehensive risk assessment and planning in the context of climate change. United Nations Office for Disaster Risk Reduction

UNISDR (2009) Terminology on disaster risk reduction

Zebisch M, Schneiderbauer S, Fritzsche K, Bubeck P, Kienberger S, Kahlenborn W, Schwan S, Below T (2021) The vulnerability sourcebook and climate impact chains—a standardised framework for a

climate vulnerability and risk assessment. Int J Clim Change Strateg Manag 13:35–59. https://doi.org/10.1108/IJCCSM-07-2019-0042

Zebisch M, Terzi S, Pittore M, Renner K, Schneiderbauer S (2022) Climate impact chains—a conceptual modelling approach for climate risk assessment in the context of adaptation planning. In: Kondrup C, Mercogliano P, Bosello F, Mysiak J, Scoccimarro E, Rizzo A, Ebrey R, de Ruiter M, Jeuken A, Watkiss P (eds) Climate Adaptation Modelling, Springer Climate. Springer, Cham, pp 217–224. https://doi.org/10.1007/978-3-030-86211-4_25

Zimmermann M, Keiler M (2015) International frameworks for disaster risk reduction: Useful guidance for sustainable mountain development? Mt Res Dev 35:195–202. https://doi.org/10.1659/MRD-JOURNAL-D-15-00006.1

Publisher's Note Springer Nature remains neutral with regard to jurisdictional claims in published maps and institutional affiliations.